Reconnaissance of Two Liquefaction Sites Using Small Unmanned Aerial Vehicles and Structure from Motion Computer Vision Following the April 1, 2014 Chile Earthquake

Kevin W. Franke, M.ASCE[1]; Kyle M. Rollins, M.ASCE[2]; Christian Ledezma, M.ASCE[3]; John D. Hedengren[4]; Derek Wolfe, S.M.ASCE[5]; Samantha Ruggles, S.M.ASCE[6]; Christopher Bender, S.M.ASCE[7]; and Brandon Reimschiissel[8]

Abstract: Small unmanned aerial vehicles (sUAVs) were used to reconnoiter, image, and model the effects of soil liquefaction at two separate sites following the M8.2 and M7.6 earthquakes near Iquique, Chile, on April 1 and 2, 2014, respectively. Geotechnical investigators performed conventional observations/measurements at the two sites using traditional reconnaissance methods, and virtual observations/measurements using sUAV-based remote sensing and structure from motion (SfM) computer vision. Two types of sUAV platform/sensor combinations were evaluated for this study. Comparisons between the traditional and sUAV-based reconnaissance methods were performed and observations are discussed. The sUAV-based point cloud models of the sites were between 770 and 2,600 points per square meter depending on the camera that was used, with average model dimensional error ranging from ±1.0 to ±3.5%. Lateral spread displacement measurements from the UAV-based three-dimensional models were generally within 9 cm of the lateral spread displacements measured in the field, and measured vertical deformations from the models generally agreed well with the deformations reported by previous investigators. This study demonstrates that sUAVs can be useful instruments for post-disaster geotechnical surficial site reconnaissance. **DOI: 10.1061/(ASCE)GT.1943-5606.0001647.** © *2016 American Society of Civil Engineers.*

Introduction

Field reconnaissance of earthquake-induced soil liquefaction and its effects is important to advance fundamental understanding of the behavior and the mechanics of liquefied soil. The recent simultaneous development of computer vision and autonomous aerial vehicles creates a new opportunity to access disaster areas for the purpose of collecting and analyzing surface geotechnical data. As with any new measurement method, it must be compared against engineering standards to validate and quantify its performance.

Researchers have carefully documented and/or compiled observations from many past liquefaction and nonliquefaction sites, resulting in various databases for liquefaction triggering case histories (e.g., Seed et al. 1985; Kayen and Mitchell 1997; Robertson and Wride 1998; Andrus and Stokoe 2000; Cetin et al. 2004; Moss et al. 2006; Boulanger et al. 2012), lateral spread displacement case histories (e.g., Bartlett and Youd 1995; Bardet et al. 2002; Youd et al. 2002), and post-liquefaction settlement case histories (e.g., Cetin et al. 2009, Juang et al. 2013). The retrieval of reliable and well-documented liquefaction reconnaissance data from the field following an earthquake can be difficult because strong ground motions typically occur over a large geographic area, thus often creating numerous potential liquefaction and nonliquefaction damage sites of interest. Additionally, surficial evidence of liquefaction, including ground cracks and sand boils, often perishes rapidly. To overcome these challenges, many researchers have investigated the application of remote sensing in collecting and analyzing geospatial data from the field immediately following an earthquake. For example, many investigators have used multispectral optical satellite imagery [with typical spatial resolutions ranging from 0.6 to 30 m (Rathje and Adams 2008)] to observe, detect, and/or measure geotechnical, structural, and/or lifeline damage from liquefaction and seismic-induced landslides (e.g., Huyck et al. 2006; Ramakrishnan et al. 2006; Rathje et al. 2006; Tang et al. 2011; Oommen et al. 2013; Xu et al. 2014; Ramakrishnan 2014). Other investigators have used aerial or terrestrial light detection and ranging (LiDAR) technology to remotely obtain data from post-liquefaction damage sites at much higher spatial resolutions [typically ranging in accuracy from 0.01 to 1.0 m

[1]Assistant Professor, Civil and Environmental Engineering, Brigham Young Univ., Provo, UT 84602 (corresponding author). E-mail: Kfranke@et.byu.edu

[2]Professor, Civil and Environmental Engineering, Brigham Young Univ., Provo, UT 84602.

[3]Assistant Professor, Pontificia Universidad Católica de Chile, Center for Integrated Natural Disaster Management CONICYT/FONDAP/15110017, Vicuña Mackenna 4860, Macul, Santiago 7820436, Chile.

[4]Assistant Professor, Chemical Engineering, Brigham Young Univ., Provo, UT 84602.

[5]Graduate Researcher, Civil and Environmental Engineering, Brigham Young Univ., Provo, UT 84602.

[6]Graduate Researcher, Civil and Environmental Engineering, Brigham Young Univ., Provo, UT 84602.

[7]Undergraduate Researcher, Civil and Environmental Engineering, Brigham Young Univ., Provo, UT 84602.

[8]Undergraduate Researcher, Electrical and Computer Engineering, Brigham Young Univ., Provo, UT 84602.

Note. This manuscript was submitted on April 4, 2016; approved on September 14, 2016; published online on December 2, 2016. Discussion period open until May 2, 2017; separate discussions must be submitted for individual papers. This paper is part of the ***Journal of Geotechnical and Geoenvironmental Engineering***, © ASCE, ISSN 1090-0241.

(Rathje and Adams 2008)] (e.g., Kayen et al. 2006; Olsen et al. 2012; Imakiire et al. 2012; Konagai et al. 2013).

A newer technology that rapidly is gaining popularity in the remote sensing community is the use of unmanned aerial vehicles (UAVs). In particular, small UAVs (sUAVs), which are commonly defined as UAV platforms that weigh less than 25 kg (55 lbs) in total weight, rapidly are gaining popularity with scientists and engineers because of the portability, relative ease of maintenance and operation, and relative affordability. A sUAV can carry one or more sensors, including various optical sensors (e.g., digital cameras, video recorders, multispectral cameras, and thermal cameras) and even small LiDAR sensors. The type and size of sensor that can be carried by a particular sUAV varies substantially, and is generally a function of the size of the platform and the desired flight endurance. One of the most common forms of remote sensing from a sUAV is the use of lightweight optical sensors with stereo photogrammetry or computer vision such as Structure from Motion (SfM) (Marr and Nishihara 1978; Snavely et al. 2008). Subcentimeter resolutions and median three-dimensional (3D) point cloud accuracies as high as 3–4 cm using SfM from sUAV-based images recently have been reported in the literature (Turner et al. 2015). Although these resolutions and accuracies are inferior to those typically obtained with survey-grade terrestrial LiDAR scanning, the ability to quickly gather data from a relatively large area with minimal ground occlusions because of the aerial point of view makes sUAV-based remote sensing an attractive alternative for many geotechnical and geological applications.

Research investigating the applied benefits and potential uses of sUAVs in the field of civil engineering has accelerated recently. For example, investigators have experimented with sUAVs to remotely measure landslides and rock fall deformations (e.g., Gong et al. 2010; Niethammer et al. 2012; Stumpf et al. 2013; Lucieer et al. 2014; Turner et al. 2015), traffic monitoring (e.g., Coifman et al. 2006; Zhou et al. 2015), road surface distress (e.g., Zhang and Elaksher 2012; Dobson et al. 2013), geological and/or topographical terrain mapping (e.g., Stefanik et al. 2011; Bemis et al. 2014), coastal monitoring (e.g., Mancini et al. 2013), bridge monitoring (e.g., Metni and Hamel 2007), pipeline monitoring (e.g., Hausamann et al. 2005; Rathinam et al. 2008), levee monitoring (e.g., de Albuquerque Nóbrega et al. 2013), and earthwork and site grading (e.g., Siebert and Teizer 2014). Some research has been performed with sUAVs to obtain site data following a major earthquake (e.g., Gong et al. 2010; Hu et al. 2012; Xu et al. 2014), but these studies generally have focused on landslide displacement and/or structural damage detection.

To the authors' knowledge, this paper presents the first documented use of sUAVs for reconnaissance of seismic-induced soil liquefaction and lateral spread following a major earthquake. Specifically, two different sUAV platforms were used to reconnoiter two separate sites in Chile that liquefied following the moment magnitude (M_w) 8.2 earthquake that occurred on April 1, 2014, and the M_w 7.6 aftershock that occurred on April 2, 2014, offshore near the cities of Iquique and Arica. Manual field surveys were performed at the two liquefaction sites, including survey tape measurements of horizontal ground deformations at select locations. Digital aerial photographs and high-definition video images were collected with the sUAV platforms, and were post-processed using SfM computer vision software to develop 3D point cloud models of the sites. Ground deformations were manually measured from the point cloud models and were compared against the surveyed deformations from the field to assess the accuracy of the point clouds. Results of these comparisons are presented in this paper, and the significance of those results to the geotechnical engineering community and their limitations are discussed.

Description of the Earthquake

The April 1, 2014, M_w 8.2 Pisagua earthquake was triggered at 20:46:45 local time, with hypocentral location 19.572°S, 70.908°W, and 38.9 km deep (Barrientos 2014). The primary seismological setting for the event was a large seismic gap that was created from large earthquakes (i.e., $M_w > 7.4$) that occurred in the region in 1868, 1877, 1967, 1995, 2001, and 2007 (Contreras-Reyes et al. 2012). An M_w 7.6 aftershock that occurred on April 3, approximately 53 km southwest of the city of Iquique, was believed by many eye witnesses to have caused more local damage than the main shock (Rollins et al. 2014).

Prior to the main shock on April 1, an earthquake swarm occurred on the same plane as the eventual main rupture (Barrientos 2014). This swarm of events had a maximum magnitude of M_w 6.7 on March 16, which triggered a tsunami evacuation warning in the city of Iquique and led to speculation on the predictability of megathrust events (Brodsky and Lay 2014). This foreshock activity gradually progressed toward the hypocentral zone.

According to the USGS (Hayes 2014), the most significant slip and energy release of the April 1 main shock occurred 34 km to the northwest of Iquique, which was the city in which the most severe infrastructure damage was observed (Rollins et al. 2014). The zone of maximum slip had a width and length of approximately 60 and 75 km, respectively, with a maximum slip on the order of 8 m. The zone of slip is outlined on the site vicinity map presented in Fig. 1.

Liquefaction Site Descriptions

Shortly following the occurrence of the April 1 and 2 earthquakes, geotechnical engineering researchers assessed liquefaction damage at ports and highway bridges in the vicinity of Iquique and Arica (Rollins et al. 2014). Two significant liquefaction and lateral spread sites were identified, and were used to experiment with sUAV-based remote sensing in this study. Fig. 1 shows the locations of these two liquefaction and lateral spread sites relative to the epicenters of the April 1 and April 2 earthquakes, and the zone of slip from the April 1 main shock.

The Molo Pier at Iquique

The Molo Pier (20.2019° S, 70.1580° W) is located approximately 105 km southeast of the epicenter of the April 1 earthquake. The pier is one of two principal piers currently used at the Port of Iquique. The pier was originally constructed in 1928, and is approximately 530-m long and 65-m wide. Rollins et al. (2014) describe the pier as consisting of large concrete block quay walls approximately 14-m high and placed on top of mounds of gravel and boulders, and likely backfilled with coarse-grained soils with little to no compactive effort.

Significant evidence of liquefaction was observed and documented across much of the Molo Pier (Rollins et al. 2014). Fig. 2 presents a photograph of the damaged pier. Cracks caused by lateral spread displacement were measured by researchers, resulting in estimated lateral ground deformations ranging from approximately 0.5 to 2.0 m. Measured post-liquefaction settlements behind the quay wall ranged from 0.8 to 1.1 m. The majority of these deformations occurred along the east quay wall of the pier. Observations also were made that lateral spread displacements appeared to continue slowly, increasing over a period of weeks following the earthquake.

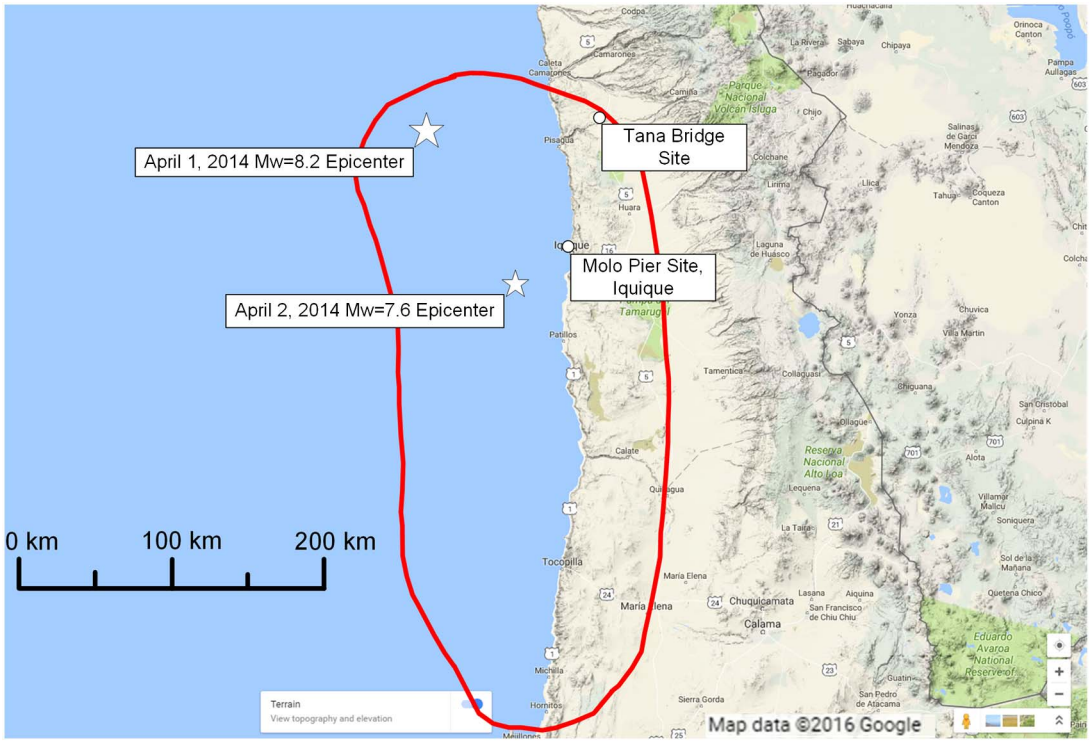

Fig. 1. Site vicinity map showing the locations of the epicenters of the April 1 and April 2 earthquakes, the Tana Bridge, and the Molo Pier (map data © 2016 Google)

The Tana Bridge

The Tana Bridge (19.4545° S, 69.9463° W) is located 103 km east of the epicenter of the April 1 earthquake. The two-lane highway bridge is located on Interstate-5 in Chile, spanning a small stream at the base of a steep desert canyon. The bridge consists of five spans of steel girders that are 16.5-m long, placed along a curve with a radius of about 100 m and transecting an arc of about 50°. Plans for the bridge suggest that the soils beneath the bridge consist primarily of poorly-graded gravel (GP) to a depth of approximately 25 m, with a surface layer of silty sand (SM) that is about 1.5-m thick (Rollins et al. 2014). The as-built plans also show that no deep foundations were used to support the bridge, but that each of the four bents is supported by a 4-m tall rectangular spread footing with base plan dimensions of 2.5-m wide by 9.6-m long. The abutments of the bridge are supported by spread footings that 3.5-m wide.

Geotechnical investigators found significant evidence of soil liquefaction and lateral spread displacement in the vicinity of the Tana Bridge following the April 1 and 2 earthquakes. Fig. 3 presents a photograph of the bridge and apparent liquefaction/lateral spread displacement evidence. Several sand boils were documented adjacent to the northern-most bent, and post-liquefaction settlements ranging from less than 15 cm to over 50 cm were observed

Fig. 2. Liquefaction and lateral spread damage near the head of the Molo Pier in Iquique, Chile (reprinted from Rollins et al. 2014, with permission)

Fig. 3. Liquefaction and lateral spread displacement at the Tana Bridge on Interstate-5 in Chile (image by K. Franke)

at the bent. Lateral spread displacements were observed on both sides of the bridge on the north and south sides of the stream. However, displacements and cracking on the east side of the bridge were much more visible because of the lack of surficial vegetation. Very large displacements and vertical slumping failures were documented on the north side of the stream, and horizontal displacements were very difficult to measure because of the extent and the severe level of distress in the ground. Vertical offsets of the slumps were measured at approximately 1.5 m, and the measurement of cumulative crack widths (i.e., the summation of the crack widths along a line that runs perpendicular to the cracks) on the south side of the stream suggested lateral spread displacements ranging from 0.8 to 2.8 m.

Despite the significant amount of liquefaction that occurred in the vicinity of the Tana Bridge, relatively little damage to the bridge was observed by geotechnical researchers (Rollins et al. 2014). There were no vertical or horizontal offsets at the span joints, nor were any significant cracks visible in the support bents or abutments. The most significant apparent damage recorded by investigators was some minor cracking approximately 3- to 6-cm wide that formed behind a terraced gabion wall at the northern abutment.

Selected sUAV Platforms and Optical Sensors

Two sUAV platforms were selected to perform the reconnaissance at the two liquefaction sites on the basis of international portability, maneuverability, and ability to carry the desired optical sensors for sufficient flight duration. Both sUAV platforms were powered with lithium-ion batteries and were operated via radio control by an experienced sUAV operator. No automated global positioning system (GPS)-based flight routines were employed during the reconnaissance effort.

The primary tradeoff between the two platforms is heavier payload with more accurate sensors (Platform B) versus lower cost and portability of the lighter weight sUAV (Platform A). This study quantifies the performance tradeoffs between the two options that are representative of a range of selections for commercial, off-the-shelf (COTS) systems.

Platform A: Quadrotor sUAV and Sensor

A small and highly portable quadrotor sUAV platform was evaluated for usefulness in liquefaction site reconnaissance in this study. The platform that was used in this study was a Phantom II quadrotor sUAV, manufactured by DJI Technologies (Shenzhen, China). This platform has a typical 15–25-min flight duration, and a recommended payload of 0.5–1.0 kg. The platform incorporates a 2-axis auto-stabilizing gyro for the mounted sensor. An additional technical feature that was incorporated in the reconnaissance effort was first person view (FPV) technology, which allowed the sUAV operator to remotely view a low-resolution image from the mounted optical sensor in real time. A photograph of the quadrotor sUAV that was used in the reconnaissance of the liquefaction sites is presented in Fig. 4(a).

The optical sensor that was used with the Phantom II quadrotor for the liquefaction reconnaissance field reconnaissance was a Hero 3+ Black Edition high-definition (HD) video recorder, manufactured by GoPro (San Mateo, California). The GoPro Hero series of cameras are lightweight (i.e., ~0.75 kg), compact cameras designed for reliable operation in extreme environments. The camera used in this study was operated at 1080p HD video shooting at 48 frames per second. The resolution of each still image in the video recording was approximately 2.76 megapixels.

One disadvantage associated with small sporting cameras such as the GoPro is that they commonly use an ultrawide angle (i.e., fisheye) lens. Such lenses cause curvature and distortion in the captured optical images to allow for more of the scene to be recorded. However, such distortion in the images can distort the 3D models produced with SfM reconstruction unless the images are first modified to correct for wide-angle distortion, or the SfM algorithm is calibrated to compensate for the image distortion during processing (e.g., Wu 2014). Rather than perform these corrections, a customized 5.4 mm flat lens was fitted to the camera that was used in this study.

Platform B: Heavy-Lift Multirotor sUAV and Sensor

A heavy-lift sUAV platform also was evaluated for its potential usefulness in reconnoitering liquefaction damage sites. The heavy-lift platform that was selected was a Skyjib Super-6 hexrotor sUAV, manufactured by Aeronavics (Raglan, New Zealand). This platform has a typical 10–15-min flight duration per battery set, and a recommended payload of 3.0–5.0 kg. The platform incorporated a 2-axis auto-stabilizing gyro for the mounted sensor. No FPV technology was used with the heavy-lift sUAV platform at the time of the study.

One key difference between Platform B and Platform A was the type and size of battery that was used. Lighter, smaller UAV

(a) (b)

Fig. 4. sUAV platforms used in the post-liquefaction reconnaissance study including: (a) DJI Technologies Phantom II quadrotor with GOPRO Hero 3+ HD video recorder; (b) Aeronavics Limited Skyjib Super-6 hexrotor with Nikon D7100 DSLR camera with 35 mm AF-S Nikkor prime lens

J. Geotech. Geoenviron. Eng., 2017, 143(5): 04016125

platforms (i.e., Platform A) typically use one or more 3-cell 12-volt batteries. Larger heavy-lift UAV platforms (i.e., Platform B) typically use one or more 6-cell 22+ volt batteries. Although size and cost are important differences between these battery types, the authors observed in this study that portability also is a critical difference. Although generally there were no difficulties in transporting the 3-cell batteries through airport security, there were considerable difficulties in transporting the 6-cell batteries. Most current airline regulations allow a ticketed airline passenger to carry up to two 6-cell batteries in his/her carry-on luggage. Despite these regulations, however, it was the authors' experience that airport security personnel repeatedly attempted to confiscate the 6-cell batteries, which would have prematurely ended any post-earthquake UAV reconnaissance for this study. The authors therefore recommend shipping all 6-cell batteries to the reconnaissance site of interest prior to mobilization to avoid any potential conflicts with airport security personnel.

The optical sensor used with the Skyjib Super-6 hexrotor for the field reconnaissance was a D7100 digital SLR (DSLR) camera, manufactured by Nikon (Tokyo). The D7100 offers 24.1 megapixel image resolution with a 23.5 by 15.6 mm DX-format sensor. An AF-S Nikkor 35 mm 1:1.8G prime lens was used with the D7100 for this study. Still JPG images were captured with the D7100 at an average frequency of one image per three seconds. A much more desirable average imaging frequency would be one image per second under normal circumstances, but the camera triggering mechanism/inertial measurement unit (IMU) experienced a malfunction that unfortunately increased the time between each captured image to approximately 3–5 seconds and resulted in a sparser point cloud model of the Tana Bridge site. Additionally, limited daylight at the site prevented more than two 15-min flights. Although RAW image formats often are desirable for computer vision applications, the JPG format was used to increase the read/write speed to the digital memory storage device onboard the camera and to minimize the possibility of any additional equipment malfunction with the limited field time that was available. All other functions on the camera were set to their respective default settings.

A photograph of the Skyjib Super-6 sUAV platform and the D7100 sensor that were used in this study is presented in Fig. 4(b).

Description of Field Reconnaissance Activities

The Molo Pier at Iquique

Rollins et al. (2014) describe in detail the field reconnaissance activities that occurred during June 2014 at the Molo Pier. A total of five cone penetration tests (CPT) were performed adjacent to two lines that ran transverse across the pier. Manual crack measurements were made along these two lines using a surveyor's tape, and cumulative lateral spread displacements were computed. A third line of crack measurements was performed at the head of the pier. A plan view layout of the field activities performed at the Molo Pier is presented in Fig. 5 (after Rollins et al. 2014).

The sUAV surveys of the Molo Pier consisted of nine consecutive 15-min flights using the Phantom II quadrotor sUAV with the GoPro Hero 3+ HD video camera. The flights were performed manually by a sUAV operator, and the sUAV captured its images from elevations ranging from 10 to 60 m above the ground, resulting in images with ground sample distances (GSDs) ranging from 1.80 to 6.02 cm/pixel, respectively. From the HD video imagery that was taken during the sUAV flights, nearly 390,000 GoPro still images of the pier were available for analysis. This large number of still images was significantly down-sampled to produce 466 still images of the pier for computer vision 3D reconstruction. No ground control points were placed at the time of the sUAV flights, but five concrete and/or steel objects at the pier were selected and measured with a total station surveying device during the summer of 2015, approximately one year after the sUAV flights at the pier. These measurements were performed with a ±2-mm horizontal accuracy and ±5-mm vertical accuracy. The selected concrete and/or steel objects ranged in size from 2.470 to 144.566 m, and were used to scale the 3D point cloud model of the pier and to assess the dimensional accuracy/error.

The Tana Bridge

Researchers performed initial observations and preliminary measurements of liquefaction effects at the Tana Bridge within one week following the April 1 and 2 earthquakes (Rolllins et al. 2014). The locations of sand boils, liquefaction-induced settlements, abutment wall damage, and lateral spread displacements were documented and a few preliminary measurements were made with a surveyor's tape. Some of these researchers returned to the Tana Bridge site again in June 2014 with sUAV equipment to assess the state of the liquefaction evidence and to perform additional, more accurate measurements of surficial liquefaction evidence. These engineers observed that the liquefaction evidence remained largely in the same condition as they had observed immediately after the earthquake, likely because of the site's remote location and very arid climate. Lateral spread displacement crack widths were measured along three lines on the east side of the bridge and south of the stream, as shown in Fig. 6. A fourth line of crack measurements also was attempted within the slump zone on the north side of the stream (shown as a dashed Line 4 in Fig. 6), but the significant ground disturbance, crumbling, and shear failures in the soil made any attempt to objectively measure horizontal crack widths and vertical deformations along this line unfeasible.

The sUAV surveys of the Tana Bridge and surrounding area consisted of two consecutive 15-min flights using the Skyjib Super-6 hexrotor sUAV with the Nikon D7100 DSLR camera. More flights could not be performed because of the malfunctioning triggering mechanism/IMU on the DSLR camera (as previously described) and because of time constraints. As a result, the final 3D point cloud model of the bridge site was sparse in several locations,

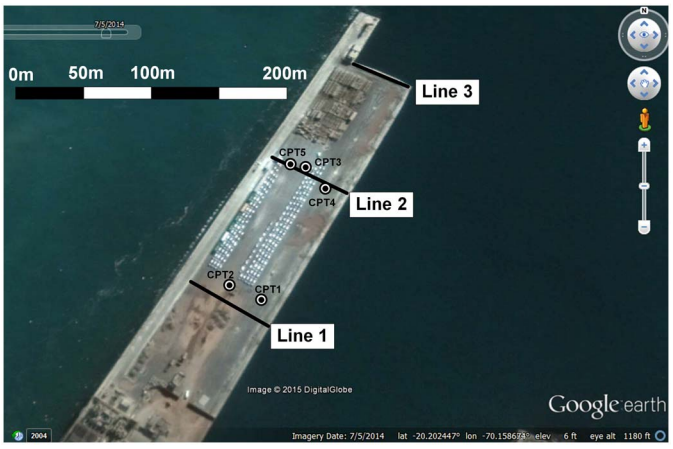

Fig. 5. Plan view layout of the geotechnical site reconnaissance activities at the Molo Pier (image © 2015 DigitalGlobe; adapted from Rollins et al. 2014)

J. Geotech. Geoenviron. Eng., 2017, 143(5): 04016125

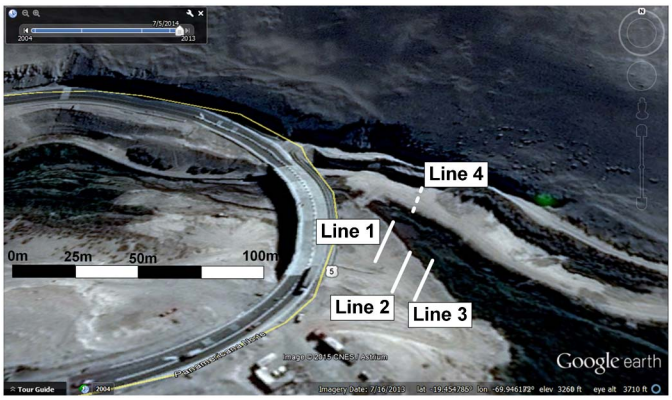

Fig. 6. Plan view layout of the geotechnical site reconnaissance activities at the Tana Bridge (Image © 2015 CNES/Astrium)

including on the bridge deck itself, and only one of the three measured lateral spread displacement lines (Line 2) appeared clearly and in its entirety in the point cloud. The sUAV flights were performed manually by a UAV operator, and the sUAV captured the images from elevations ranging from 5 to 60 m above ground, resulting in images with GSDs ranging from 0.06 to 0.63 cm/pixel, respectively. In total, 622 useable DSLR still images of the bridge and surrounding area were captured from the sUAV flights. As previously, no ground control points were placed at the time of the sUAV flights, but five concrete objects at the bridge were selected and measured with a total station surveying device during the summer of 2015, approximately one year after the original sUAV flights. These measurements were performed with a ±2-mm horizontal accuracy and ±5-mm vertical accuracy. The selected objects ranged in size from 1.131 to 11.562 m, and were used to scale the 3D point cloud model of the bridge site and to assess its dimensional accuracy/error.

Computer Processing and 3d Model Development

The SfM computer vision image processing was performed using the commercial 3D visualization software *PhotoScan 1.1.6*. The customized computer workstation used to operate *PhotoScan* uses two Intel (Santa Clara, California) Xeon i7 E5-2680 v2 CPUs at 2.80 GHz, with 256 GB of double data rate (DDR) random access memory (RAM) and two nVidia GeFORCE GTX 780 Ti graphics cards. With this set of workstation specifications, processing times to develop 3D point clouds and meshed surface models were generally less than 24 h for each of the two sites.

The SfM workflow that was used to develop 3D point clouds and meshed models consisted of the recommended general workflow for *PhotoScan* (Agisoft 2014), with some minor variations. Images from each of the two liquefaction sites first were preprocessed to evaluate them for excessive blur, overexposure, reflective surfaces, and/or excessive data outside the area of interest. Images found with these undesirable qualities were removed from the image set. This step required approximately 4–6 h per image set to complete. Image sets from each sUAV platform next were uploaded to *PhotoScan*. Overall, 466 images were uploaded to *PhotoScan* to develop the Molo Pier model, and 622 images were uploaded to develop the Tana Bridge model. High accuracy processing and aggressive depth filtering were specified in *PhotoScan*, and a maximum point limit was set at 200 million. The time required to develop the dense 3D point clouds ranged from 6 to 12 h for the two individual models. Meshed (i.e., textured) models then were built for each of the dense point cloud models within *PhotoScan*

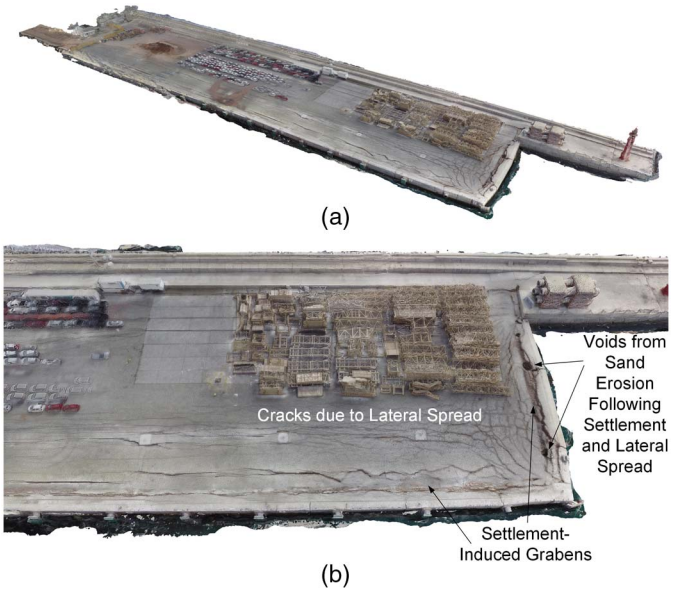

Fig. 7. sUAV-based computer vision 3D point clouds of (a) the entire Molo Pier; (b) a close-up of the heavily damaged head of the pier

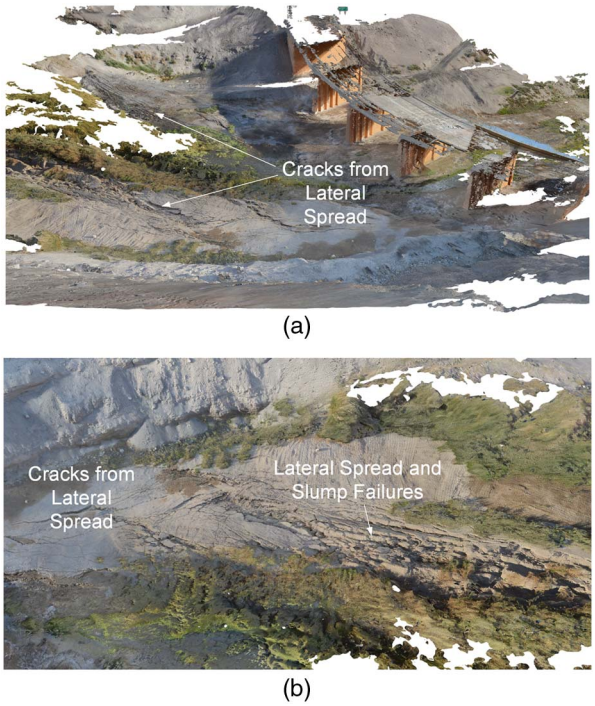

Fig. 8. sUAV-based computer vision 3D point clouds of (a) the Tana Bridge site (looking to the south); (b) a close-up of the lateral spread and slump zone on the north side of the stream (looking to the north)

for the purpose of manually measuring lateral spread-induced ground cracks, which required another 10–12 h of processing time per model. Finalized dense point clouds were exported as polygon file format (PLY) files to be scaled, edited, and analyzed in point cloud manipulation software *CloudCompare 2.6.1* and *I-Site Studio 5.1*.

Images of the resulting dense point cloud models for the Molo Pier and the Tana Bridge are presented in Figs. 7 and 8, respectively. The total number of points in the dense point clouds was

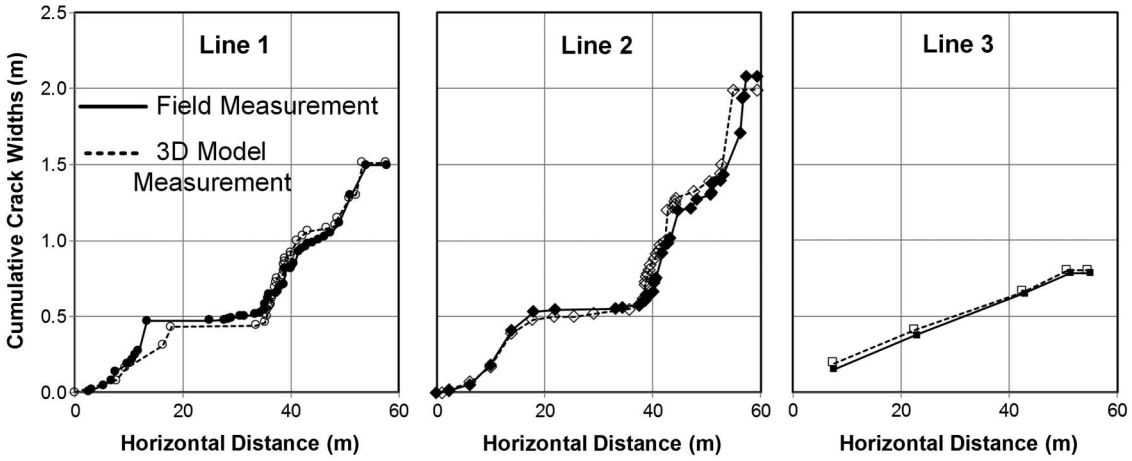

Fig. 9. Crack width comparisons between actual field measurements and virtual measurements from the UAV-based 3D point cloud model of the Molo Pier

13,928,047 points in the Molo Pier model, and 117,023,873 points in the Tana Bridge model. The total number of meshed faces on the meshed models was 2,785,609 in the Molo Pier model and 35,404,756 faces in the Tana Bridge model. Analysis of the dense point clouds revealed an average point resolution of 770 points per square meter in the Molo Pier model, and an average point resolution of 2,600 points per square meter in the Tana Bridge model. Thus, the disadvantage of using a smaller, lower-resolution camera like the GoPro instead of a DSLR in the 3D virtual site reconstruction is apparent in the lower point resolution of the Molo Pier point cloud model. Additional factors such as focal length of the lens, distance from the lens to the ground surface, image overlap, velocity of the sUAV, and the total number of images also will impact significantly the quality of a 3D virtual site reconstruction.

Point cloud dimensional accuracy evaluations were performed by comparing the model dimensions of the selected field objects with the actual field measurements. From these comparisons, the observed average dimensional error for the Molo Pier model was $\pm 2.5\%$, with a maximum observed dimensional error of 3.5%. The observed average dimensional error for the Tana Bridge model was $\pm 1.0\%$, with a maximum observed dimensional error of -2.1%. Thus, the superior lens, image quality, and imaging sensor of the DSLR camera contributed to a better average model dimensional accuracy (by approximately a factor of 3.5) over the GoPro-based model. Similar findings have been documented in other UAV remote sensing studies (e.g., Ruggles et al. 2016). These accuracies would have been improved further had GPS-surveyed ground control points been incorporated into the computer vision workflow (Agisoft 2014). However, the incorporation of surveyed ground control points also would have increased the time required to complete the field work at each site, perhaps by a factor of two or three. Therefore, there is a tradeoff between model accuracy and field work time that an engineer must consider when performing UAV-based remote sensing with computer vision.

Comparisons between UAV-Based Measurements and Actual Measurements of Lateral Spread Displacement

Once the 3D point cloud and meshed models of both the Molo Pier liquefaction site and the Tana Bridge liquefaction site were developed and scaled, cumulative crack displacements were manually

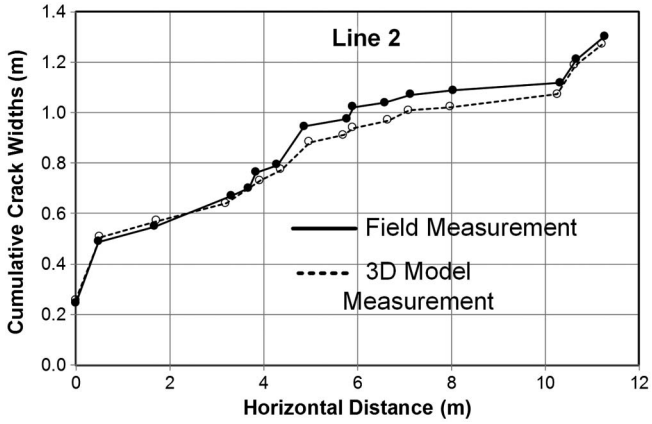

Fig. 10. Crack width comparisons between actual field measurements and virtual measurements from the UAV-based 3D point cloud model of the Tana Bridge

measured in the meshed models using *Memento Beta* at each location in which corresponding crack width measurements were performed in the field. As previously stated, only one of the three lines of crack width measurements (Line 2) could be measured in the Tana Bridge model because of the sparseness of the point cloud at the other two line locations. The resulting comparisons between the virtual (i.e., UAV model) and actual (i.e., measured) cumulative crack widths at the Molo Pier and the Tana Bridge sites are presented in Figs. 9 and 10, respectively.

Fig. 9 shows the cumulative crack width comparisons. The measurements taken from the Molo Pier meshed model captured the overall displacement pattern measured in the field and generally were within 0.3 m of the actual field measurements at any location. Additionally, the total cumulative crack width measurements taken from the meshed model were within 0.09 m of the actual field measurements at all three lines. As expected, the disparity between the model crack width measurements and the actual field measurements was even smaller at the Tana Bridge site (shown in Fig. 10), at which the higher-quality D7100 DSLR camera was used with the sUAV. The measurements taken from the Tana Bridge meshed model generally were within 0.1 m of the actual field measurements at any location, and the total cumulative crack width measurement

J. Geotech. Geoenviron. Eng., 2017, 143(5): 04016125

for the single line that was visible was within 0.05 m of the actual field measurement.

Assessment of Vertical Ground Deformations

Three-dimensional point clouds developed from sUAV-based SfM computer vision also can be used to assess vertical ground deformations at liquefaction sites. For example, a digital elevation model (DEM) can be developed from a 3D point cloud, allowing for vertical ground deformation analysis through comparison with a pre-earthquake DEM in a traditional geographic information system (GIS). Alternatively, pre- and post-earthquake 3D point clouds can be used directly to estimate vertical deformations through 3D point differencing. Such an approach requires the coregistration and alignment of the pre- and post-earthquake 3D point clouds to a local coordinate system, usually using the iterative closest point (ICP) algorithm (Besl and McKay 1992) or one of its variations (e.g., Zhang et al. 2015). If no pre-earthquake point cloud of the site of interest is available (as with this study), then an estimated pre-earthquake ground surface profile can be used with the post-earthquake 3D point cloud to estimate the vertical deformations that occurred during the earthquake.

Fig. 11 presents ground surface profiles developed from the 3D point cloud across the liquefaction-induced graben along the eastern side of the Molo Pier for Lines 1, 2, and 3. Also drawn on these figures is the assumed horizontal ground surface from before the earthquake (shown as a dashed line). From each of these profiles, the maximum measured vertical deformations along the lines are 1.14, 0.98, and 0.82 m for Lines 1, 2, and 3, respectively. These values compared well with the observed vertical deformation range of 0.8 to 1.1 m reported by geotechnical extreme events reconnaissance (GEER) investigators (Rollins et al. 2014). However, deviations from the assumed of a horizontal pre-earthquake ground surface could induce some errors in measured vertical deformations.

Three-dimensional point cloud and meshed models of the Tana Bridge also are useful for evaluating vertical ground deformations at the bridge site. For example, Rollins et al. (2014) reported that a number of liquefaction surface features and evidence of liquefaction-induced settlement were visible adjacent to the northern pier of the bridge. An approximate vertical offset of 15 cm because of the liquefaction-induced settlement was reported. This liquefaction-induced vertical offset was still visible two months after the initial GEER team reconnoitered the site, and is shown in Fig. 12(a), which is a digital photograph captured by the sUAV-mounted DSLR camera. Using the 3D-meshed SfM model of the site presented in Fig. 12(b), vertical offsets were measured carefully along the liquefaction-induced settlement feature at the bridge bent. Model measurements showed that the vertical offsets increased linearly from 0 cm of settlement midway between the bent and the northern abutment to 51 cm of maximum settlement adjacent to the bent. Therefore, the average vertical offset was approximately 25 cm, which is greater than the reported offset of 15 cm

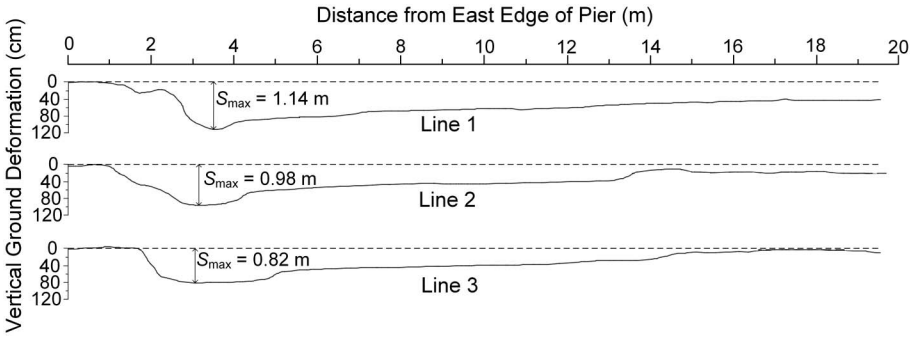

Fig. 11. UAV-based vertical deformation profiles along Lines 1, 2, and 3 at the Molo Pier

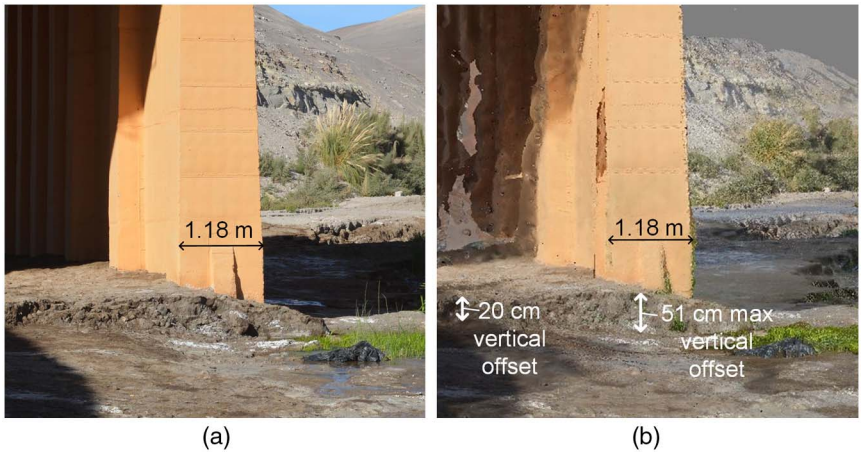

Fig. 12. Post-liquefaction ground settlement at the western side of the northern bent of the Tana Bridge: (a) digital photograph of the settlement taken from the UAV-based DSLR camera; (b) 3D meshed simulation of the bent shown in Part (a) with settlement measurements

J. Geotech. Geoenviron. Eng., 2017, 143(5): 04016125

by Rollins et al. (2014). A possible explanation for this discrepancy might be that additional ground settlement occurred between the time of the initial GEER reconnaissance in April 2014 and the sUAV reconnaissance in June 2014. It is also possible that the initial GEER researchers simply measured the vertical offsets in a different location that produced the 15 cm settlement estimate. Regardless, Fig. 12 demonstrates the potential usefulness of a 3D point cloud and/or meshed model in validating initial displacement estimates obtained by field reconnaissance investigators.

Discussion and Limitations

The liquefaction and lateral spread case histories presented in this paper effectively demonstrate the tremendous potential for using sUAVs to perform surficial postdisaster geotechnical reconnaissance. The authors recognize that each method of remote sensing, including sUAV-based photographic imaging, has strengths and weaknesses (Rathje and Adams 2008). However, sUAV-based remote sensing appears to provide a sensible balance between acquisition/maintenance costs, portability, visibility, model resolution, and accuracy. Imaging technology continues to progress with novel advancements, such as mirrorless DSLR cameras (significantly lighter and smaller than traditional DSLR cameras). A combination of hardware and software advances will continue to introduce more useful, versatile, and affordable remote sensing alternatives.

The authors acknowledge that the 3D point clouds presented in this paper closely resemble the 3D point clouds that one might obtain using LiDAR (terrestrial or low-altitude aerial) technology, which has been in existence for several years. Some engineers, therefore, might question the value and/or novelty of the results presented in this study. The value and novelty of this work is not necessarily in the 3D point cloud models themselves, but rather in how those 3D point clouds were generated. The application of SfM computer vision and sUAV technologies in surficial geotechnical remote sensing offers two significant advantages over traditional LiDAR remote sensing methods: equipment cost and field time. The only sensor required to perform SfM computer vision is a single commercial off-the-shelf digital camera, which is usually at least one order of magnitude less expensive than a typical LiDAR scanner and much easier to replace if broken. Although the models presented in this paper were processed on a local computer workstation, many commercial SfM software packages now allow all computer vision processing to be performed in the cloud, thus reducing the need for engineers to own or operate their own workstation. Because of the maneuverability and improved low-altitude viewpoint of the sUAV, an experienced field operator often can collect all necessary images to reconstruct a 3D point cloud model in a fraction of the time that is required to perform terrestrial LiDAR scanning, particularly if significant occlusions are present on the ground. However, the inclusion of ground control points in a sUAV-based SfM computer vision model can increase significantly the amount of field time required for reconnaissance because each ground control point must be surveyed with traditional survey equipment (e.g., GPS or total station).

The results presented in this study were developed from reconnoitering two separate liquefaction sites with small UAVs following a major earthquake event. Although the results presented in this paper are promising and show significant potential for sUAV-based postdisaster geotechnical surface site reconnaissance, they understandably are limited and would benefit from additional assessment of the technology following future disaster events. Future postdisaster reconnaissance missions, therefore, should strongly consider the inclusion of sUAV technology in their field activities to further evaluate its merits, advantages, and limitations.

Conclusions

This paper demonstrated the use of two different sUAV platforms and digital cameras for the image-based reconnaissance and subsequent 3D surface model generation of two liquefaction sites following the M_w 8.2 April 1 Pisagua earthquake near Iquique, Chile, using SfM computer vision techniques. The Molo Pier in Iquique experienced lateral spread displacements, ranging from 0.5 to 2.0 m, and liquefaction-induced vertical ground displacements behind the displaced quay walls, ranging from 0.8 to 1.1 m. The Tana Bridge site on Interstate-5 between Iquique and Arica experienced lateral spread displacements, ranging from 0.8 to 2.8 m, and liquefaction-induced ground settlements adjacent to the northern pier of the bridge of approximately 15 cm or greater.

A DJI Phantom II quadrotor sUAV platform mounted with a GoPro Hero 3+ digital video recorder was flown at the Molo Pier, and Aeronavics Skyjib Super-6 hexrotor sUAV mounted with a Nikon D7100 DSLR camera was flown at the Tana Bridge site. Various measurements of lateral spread displacement and vertical ground offsets were performed at each of two liquefaction sites. Three-dimensional point cloud and meshed models of the two liquefaction sites were developed from the sUAV-based images collected from the field using the SfM software *PhotoScan*, and were scaled to proper size using the software *CloudCompare* and *Memento Beta.* Comparisons with actual surveyed objects from the field suggested that the 3D model of the Molo Pier had an average dimensional error of $\pm 2.5\%$ in the model, with a maximum observed dimensional error of 3.5%. Similar comparisons with the 3D model of the Tana Bridge site suggest an average dimensional error of $\pm 1.0\%$, with a maximum observed dimensional error of -2.1%.

Virtual crack width measurements from the Molo Pier 3D model (developed from the GoPro Hero 3+ still images) were within 0.09 m of the actual total field measurements. Virtual crack width measurements from the Tana Bridge site model (developed from the Nikon D7100 DSLR images) were within 0.05 m of the actual total field measurements. Vertical ground deformations measured from the Molo Pier model generally confirmed the reported post-liquefaction vertical deformations by the initial GEER reconnaissance team (Rollins et al. 2014). Vertical ground deformations at the northern pier measured from the Tana Bridge model were significantly larger than the deformations reported by the initial GEER reconnaissance team. This discrepancy could be because of additional settlements occurring at the site between April 2014 and June 2014, or because of the reported settlement being measured at a different location near the bridge bent. On the basis of the results presented in this study, sUAV-based computer vision modeling may be considered among the most accurate remote sensing methods for recording and measuring surface ground deformations from seismic-induced soil liquefaction.

Acknowledgments

Funding for this study was provided in part by the National Science Foundation (NSF) Industry/University Cooperative Research Center for Unmanned Aircraft Systems (C-UAS) through Project No. BYU13-03; the Geotechnical Extreme Events Reconnaissance (GEER), which is funded through the NSF Geotechnical Engineering Program under Grant No. CMMI-1266418; and NSF Grant No.

CMMI-1235526. C. Ledezma was funded by the Chilean Fondo Nacional de Desarrollo Científico y Tecnológico (FONDECYT) under Grant No. 11110125. This support is gratefully acknowledged. However, the views and opinions expressed do not necessarily represent those of the NSF, C-UAS, GEER, or FONDECYT. The authors also gratefully acknowledge the assistance of their fellow GEER researchers that helped investigate and document the geotechnical damage from the April 1 Iquique earthquake, particularly Professors Gonzalo Montalva (Universidad de Concepción) and Esteban Sáez (Pontificia Universidad Católica de Chile).

References

Agisoft. (2014). "Agisoft photoscan user manual: Professional edition." ⟨http://www.agisoft.com/pdf/photoscan-pro_1_1_en.pdf⟩ (Jun. 2, 2015).

Andrus, R. D., and Stokoe, K. H., II (2000). "Liquefaction resistance of soils from shear-wave velocity." *J. Geotech. Geoenviron. Eng.*, 10.1061/(ASCE)1090-0241(2000)126:11(1015), 1015–1025.

Bardet, J. P., Tobita, T., Mace, N., and Hu, J. (2002). "Regional modeling of liquefaction-induced ground deformation." *Earthquake Spectra*, 18(1), 19–46.

Barrientos, S. (2014). "Informe técnico terremoto de Iquique, Mw=8.2, 1 de Abril de 2014." ⟨http://www.sismologia.cl/⟩ (Jan. 15, 2016).

Bartlett, S. F., and Youd, T. L. (1995). "Empirical prediction of liquefaction-induced lateral spread." *J. Geotech Eng.*, 10.1061/(ASCE)0733-9410(1995)121:4(316), 316–329.

Bemis, S. P., et al. (2014). "Ground-based and UAV-based photogrammetry: A multi-scale, high-resolution mapping tool for structural geology and paleoseismology." *J. Struct. Geol.*, 69(A), 163–178.

Besl, P. and McKay, N. (1992). "A method for registration of 3-D shapes." *IEEE Trans. Pattern Anal. Mach. Intell.*, 14(2), 239–256.

Boulanger, R. W., Wilson, D. W., and Idriss, I. M. (2012). "Examination and reevaluation of SPT-based liquefaction triggering case histories." *J. Geotech. Geoenviron. Eng.*, 10.1061/(ASCE)GT.1943-5606.0000668, 898–909.

Brodsky, E. E., and Lay, T. (2014). "Recognizing foreshocks from the 1 April 2014 Chile earthquake." *Science*, 344(6185), 700–702.

Cetin, K. O., et al. (2004). "SPT-based probabilistic and deterministic assessment of seismic soil liquefaction potential." *J. Geotech. Geoenviron. Eng.*, 10.1061/(ASCE)1090-0241(2004)130:12(1314), 1314–1340.

Cetin, K. O., Bilge, H. T., Wu, J., Kammerer, A. M., and Seed, R. B. (2009). "Probabilistic model for the assessment of cyclically induced reconsolidation (volumetric) settlements." *J. Geotech. Geoenviron. Eng.*, 10.1061/(ASCE)1090-0241(2009)135:3(387), 387–398.

CloudCompare version 2.4 [Computer software]. CloudCompare, Provo, UT.

Coifman, B., McCord, M., Mishalani, R. G., et al. (2006). "Roadway traffic monitoring from an unmanned aerial vehicle." *IEEE Proc., Int. Transp. Syst.*, 153(1), 11–20.

Contreras-Reyes, E., Jara, J., Grevemeyer, I., Ruiz, S., and Carrizo, D. (2012). "Abrupt change in the dip of the subducting plate beneath north Chile." *Nat. Geosci.*, 5(5), 342–345.

de Albuquerque Nóbrega, R. A., Aanstoos, J., Gokaraju, B., Mahrooghy, M., Dabirru, L., and O'Hara, C. G. (2013). "Mapping weaknesses in the Mississippi River levee system using multi-temporal UAVSAR data." *Revista Brasileira do Cartografia*, 65(4), 681–694.

Dobson, R. J., Brooks, C., Roussi, C., and Colling, T. (2013). "Developing an unpaved road assessment system for practical deployment with high-resolution optical data collection using a helicopter UAV." *Proc., 2013 Int. Conf. Unmanned Aircraft System*, ICUAS Association, Denver, 235–243.

Gong, J. H., et al. (2010). "Earthquake-induced geological hazard detection under hierarchical stripping classification framework in the Beichuan area." *Landslides*, 7(2), 181–189.

Hausamann, D., Zirnig, W., Schreier, G., and Strobl, P. (2005). "Monitoring of gas pipelines–Acivil UAV application." *Aircr. Eng. Aerosp. Technol.*, 77(5), 352–360.

Hayes, G. (2014). "Updated finite fault results for the Apr. 1, 2014 Mw 8.2 99 km NW of Iquique, Chile earthquake (Version 2)." ⟨http://earthquake.usgs.gov/archive/product/finite-fault/usc000nzvd/us/1397258114263/c000nzvd.html⟩ (Jun. 1, 2015).

Hu, J. P., Wu, W. B., and Tan, Q. L. (2012). "Application of unmanned aerial vehicle remote sensing for geological disaster reconnaissance along transportation lines: A case study." *Appl. Mech. Mater.*, 226, 2376–2379.

Huyck, C., Matsuoka, M., Takahashi, Y., and Vu, T. (2006). "Reconnaissance technologies used after the 2004 Niigata-ken Chuetsu, Japan, earthquake." *Earthquake Spectra*, 22(S1), 133–145.

Imakiire, T., and Koarai, M. (2012). "Wide-area land subsidence caused by the 2011 off the Pacific Coast of Tohoku earthquake." *Soils Found.*, 52(5), 842–855.

I-Site Studio version 5.1 [Computer Software]. Maptek, Inc., Denver.

Juang, C. H., Ching, J., Wang, L., Khoshnevisan, S., and Ku, C.-S. (2013). "Simplified procedure for estimation of liquefaction-induced settlement and site-specific probabilistic settlement exceedance curve using cone penetration test (CPT)." *Can. Geotech. J. Ottawa.*, 50(10), 1055–1066.

Kayen, R. E., and Mitchell, J. K. (1997). "Assessment of liquefaction potential during earthquakes by Arias intensity." *J. Geotech. Geoenviron. Eng.*, 10.1061/(ASCE)1090-0241(1997)123:12(1162), 1162–1174.

Kayen, R. E., Pack, R., Bay, J., Sugimoto, S., and Tanaka, H. (2006). "Ground-LIDAR visualization of surface and structural deformation of the Niigata Ken Chuetsu, 23 October 2004, earthquake." *Earthquake Spectra*, 22(S1), 147–162.

Konagai, K., Kiyota, T., Suyama, S., Asakura, T., Shibuya, K., and Eto, C. (2013). "Maps of soil subsidence for Tokyo bay shore areas liquefied in the March 11th, 2011 off the Pacific Coast of Tohoku earthquake." *Soil Dyn. Earthquake Eng.*, 53, 240–253.

Lucieer, A., de Jong, S. M., and Turner, D. (2014). "Mapping landslide displacements using structure from motion (SfM) and image correlations of multi-temporal UAV photography." *Prog. Phys. Geogr.*, 38(1), 97–116.

Mancini, F., Dubbini, M., Gattelli, M., Stecchi, F., Fabbri, S., and Gabbianelli, G. (2013). "Using unmanned aerial vehicles (UAV) for high-resolution reconstruction of topography: The structure from motion approach on coastal environments." *Remote Sens.*, 5(12), 6880–6898.

Marr, D., and Nishihara, H. K. (1978). "Representation and recognition of the spatial organization of three-dimensional shapes." *Proc., Royal Soc. London B*, 200(1140), 269–294.

Memento Beta [Computer Software]. Autodesk, Inc., San Rafael, CA.

Metni, N. and Hamel, T. (2007). "A UAV for bridge inspection: Visual serving control law with orientation limits." *Automat. Construct.*, 17(1), 3–10.

Moss, R. E., et al. (2006). "CPT-based probabilistic and deterministic assessment of in situ seismic soil liquefaction potential." *J. Geotech. Geoenviron. Eng.*, 10.1061/(ASCE)1090-0241(2006)132:8(1032), 1032–1051.

Niethammer, U., James, M. R., Rothmund, S., Travelletti, J., and Joswig, M. (2012). "UAV-based remote sensing of the Super-Sauze landslide: Evaluation and results." *Eng. Geol.*, 128(SI), 2–11.

Olsen, M. J., et al. (2012). "Damage assessment of the 2010 Chile earthquake and tsunami using terrestrial laser scanning." *Earthquake Spectra*, 28(S1), S179–S197.

Oommen, T., Baise, L. G., Gens, R., Prakash, A., and Gupta, R. P. (2013). "Documenting earthquake-induced liquefaction using satellite remote sensing image transformations." *Env. Eng. Geosci.*, 19(4), 303–318.

PhotoScan 1.1.6 [Computer Software], St. Petersburg, Russia, Agisoft, LLC.

Ramakrishnan, D. (2014). "Spectral discrimination of recent sediments round Bhuj, India, using Landsat-TM data and assessment of their vulnerability to seismicity-related failures." *Nat. Hazards*, 70(1), 485–499.

Ramakrishnan, D., Mohanty, K. K., and Nayak, S. R. (2006). "Mapping the liquefaction induced soil moisture changes using remote sensing technique: an attempt to map the earthquake induced liquefaction around Bhuj, Gujarat, India." *Geotech. Geol. Eng.*, 24(6), 1581–1602.

Rathinam, S., Kim, Z. W., and Sengupta, R. (2008). "Vision-based monitoring of locally linear structures using an unmanned aerial vehicle." *J. Infrastruct. Syst.*, 10.1061/(ASCE)1076-0342(2008)14:1(52), 52–63.

Rathje, E. M., and Adams, B. J. (2008). "The role of remote sensing in earthquake science and engineering: Opportunities and challenges." *Earthquake Spectra*, 24(2), 471–492.

Rathje, E. M., Kayen, R., and Woo, K. S. (2006). "Remote sensing observations of landslides and ground deformation from the 2004 Niigata Ken Chuetsu earthquake." *Soils Found.*, 46(6), 831–842.

Robertson, P. K., and Wride, C. E. (1998). "Evaluating cyclic liquefaction potential using the cone penetration test." *Can. Geotech. J.*, 35(3), 442–459.

Rollins, K., Ledezma, C., and Montalva, G., eds. (2014). "Geotechnical aspects of April 1, 2014, M8.2 Iquique, Chile Earthquake." ⟨http://www.geerassociation.org/⟩ (Jan. 15, 2016).

Ruggles, S., et al. (2016). *Comparison of SfM computer vision point clouds of a landslide derived from multiple small UAV platforms and sensors compared to a TLS-based model*, NRC Research Press, Ottawa.

Seed, H. B., Tokimatsu, K., Harder, L. F., Jr., and Chung, R. (1985). "Influence of SPT procedures in soil liquefaction resistance evaluations." *J. Geotech. Eng.*, 10.1061/(ASCE)0733-9410(1985)111:12(1425), 1425–1445.

Siebert, S., and Teizer, J. (2014). "Mobile 3D mapping for surveying earthwork projects using an unmanned aerial vehicle (UAV) system." *Automat. Constr.*, 41, 1–14.

Snavely, N., Seitz, S. M., and Szeliski, R. (2008). "Modeling the world from internet photo collections." *Inter. J. Comp. Vision*, 80(2), 189–210.

Stefanik, K. V., Gassaway, J. C., Kochersberger, K., and Abbott, A. L. (2011). "UAV-based stereo vision for rapid aerial terrain mapping." *Giscience Remote Sens.*, 48(1), 24–49.

Stumpf, A., Malet, J. P., Kerle, N., Niethammer, U., and Rothmund, S. (2013). "Image-based mapping of surface fissures for the investigation of landslide dynamics." *Geomorphology*, 186, 12–27.

Tang, C., Zhu, J., Qi, X., and Ding, J. (2011). "Landslides induced by the Wenchuan earthquake and the subsequent strong rainfall event: A case study in the Beichuan area of China." *Eng. Geol.*, 122(1–2), 22–33.

Turner, D., Lucieer, A., and de Jong, S. M. (2015). "Time series analysis of landslide dynamics using an unmanned aerial vehicle." *Rem. Sens.*, 7(2), 1736–1757.

Wu, C. (2014). "Critical configurations for radial distortion self-calibration." *Proc., Computer Vision and Pattern Recognition (CVPR), 2014 IEEE Conf.*, IEEE, New York, 25–32.

Xu, C., Xu, X. W., Yao, W., and Dai, F. C. (2014). "Three (nearly) complete inventories of landslides triggered by the May 12, 2008, Wenchuan Mw 7.9 earthquake of China and their spatial distribution statistical analysis." *Landslides*, 11(3), 441–461.

Xu, Z. Q., et al. (2014). "Development of an UAS for post-earthquake disaster surveying and its application in Ms7.0 Lushan Earthquake, Sichuan, China." *Comput. Geosci.*, 68, 22–30.

Youd, T. L., Hansen, C. M., and Bartlett, S. F. (2002). "Revised multilinear regression equations for prediction of lateral spread displacement." *J. Geotech. Geoenviron. Eng.*, 10.1061/(ASCE)1090-0241(2002)128:12(1007), 1007–1017.

Zhang, C. S., and Elaksher, A. (2012). "An unmanned aerial vehicle-based imaging system for 3D measurement of unpaved road surface distresses." *Comput. Aided Civ. Infrastruct. Eng.*, 27(2), 118–129.

Zhang, X., Glennie, C., and Kusari, A. (2015). "Change detection from differential airborne LiDAR using a weighted anisotropic iterative closest point algorithm." *IEEE J. Selected Topics Appl. Earth Obs. Remote Sensing 2015*, 8(7), 1–9.

Zhou, H. L., Kong, H., Wei, L., Creighton, D., and Nahavandi, S. (2015). "Efficient road detection and tracking for unmanned aerial vehicle." *IEEE Trans. Intell. Transp. Syst.*, 16(1), 297–309.